



ORIGINAL RESEARCH ARTICLE

Numerical Prediction of Tool Rotation Speed for Optimum Mechanical Properties of Weld Joint in Friction Stir Welding of Dissimilar Aluminum Alloys

R.S. Anand, Nishant, S.K. Jha, and P. Prakash

Submitted: 1 October 2023 / Revised: 30 March 2024 / Accepted: 20 April 2024

This research paper describes a numerical approach for determining the optimal tool rotation speed (TRS) to achieve superior mechanical properties in friction stir welding (FSW) of dissimilar aluminum alloys, specifically AA5083-H12 and AA6061-T6. For this purpose, computational fluid dynamics (CFD) coupled with the volume of fluid (VOF) method is employed to develop a numerical model for FSW. The temperature and material flow numerical model are simulated at five different TRS (710, 900, 1120, 1400, and 1600 rpm), the model explores temperature, material flow variations, and slip rates with different TRS levels. The mechanical properties are correlated with numerical analysis. Results indicate that material flow velocity near the shoulder increases as increases the TRS from 700 to 1600 rpm. However, the trend in material flow velocity changes after reaching 1120 rpm near the bottom of the tool-workpiece interface. This decrement is attributed to temperature-induced material accumulation and slip rate affecting the uniformity of contact conditions at the tool-workpiece interface. Near the bottom of the weld, slip rates increase initially with TRS from 710 to 1120 rpm but decrease thereafter. Lower slip rates at 1400 and 1600 rpm indicate increased sliding, leading to defects and reducing the tensile strength in weld joints. Optimal tensile strength of 174 MPa and an improved ductile fracture mode compared to all weld joints is obtained at 1120 rpm.

Keywords computational fluid dynamics, friction stir welding, tool rotation speed, material flow, mechanical properties, temperature distribution, weld zone formation

1. Introduction

In the last decade, Friction Stir Welding (FSW) has gained significant attention and recognition in the field of welding of similar aluminum alloy components of automobiles, shipbuilding, and aerospace to industry (Ref 1-3). Nowadays, the application FSW process is extended to joining dissimilar material due to several advantages over conventional welding techniques (Ref 4, 5). FSW offers the advantage of being a highly versatile process, as it can be applied to a wide range of materials, including aluminum, steel, titanium, copper, and their alloys, opening doors for diverse industrial applications (Ref 6, 7). FSW, an established solid-state welding method, incorporates elements of temperature, mechanics, metallurgical, and material interactions. It has emerged as a groundbreaking welding technique due to its energy efficiency, environmentally friendly nature, and ability to produce high-quality welds (Ref

8). Additionally, the state-of-the-art friction-based welding techniques are defined by low peak temperatures, inducing significant plastic deformation, energy efficiency, and environmental sustainability. These methods have the capability to achieve both mechanical and chemical bonding concurrently, leading to enhanced mechanical performance (Ref 9). However, due to different mechanical properties of the joining material, there are issues and challenges for selection of proper input process parameters for producing the dissimilar weld joint with optimum mechanical properties. In FSW several process parameters such as tool rotation speed, welding speed, plunge depth, axial force plays a crucial role in achieving good welds joint (Ref 10, 11). Among these TRS is one of the critical input process parameters which control the generation of heat, material mixing and stirring of the material around the rotating tool pin (Ref 12). Which finally, affects the weld joint formation and mechanical properties.

Many authors have reported that the selection of optimal TRS is one of the important input process parameters for achieving the good quality of the weld joints (Ref 13, 14). Rodriguez et al. (Ref 15) experimentally analyze dissimilar butt joints between AA 6061 and AA 7050 in FSW, highlighting the correlation between TRS (270, 340, and 410 rpm), material intermixing, and joint strength. Their findings demonstrate that increasing TRS enhances material intermixing and improves tensile strength of the weld joint, indicating a positive relationship between these factors. Zhang et al. (Ref 16) experimentally investigated the effect of TRS (600-1650 rpm) on microstructure, material flow, and mechanical properties in FSW joints between AA7075-T651 and AA2024-T351, to show the correlations between TRS and weld quality param-

R.S. Anand, Department of Mechanical Engineering, Birla Institute of Technology, Patna Campus, Patna, Bihar 800014, India; and Nishant, S.K. Jha, and P. Prakash, Department of Production and Industrial Engineering, Birla Institute of Technology, Mesra, Ranchi, Jharkhand 835215, India. Contact e-mail: prashantprakash@bitmesra.ac.in.

eters. Their findings aid in optimizing FSW parameters and improving joint performance, indicating an initial increase in mechanical properties with TRS until reaching peak values, with optimum properties observed at 900 rpm. Abolusoro et al. (Ref 17) experimentally explore the impact of TRS (1250-1850 rpm) on temperature distribution, mechanical behavior, and microstructure in FSW of dissimilar aluminum alloys 6101-T6 and 7075-T651, elucidating correlations between TRS, on temperature profiles, mechanical properties, and microstructural features. Their findings offer insights for defect-free welds and effective temperature feedback control in industrial applications, highlighting a rise in temperature with increased TRS and an optimal mixing observed at 1550 rpm, while tensile strength decreases with higher TRS. Zhang and Zhang (Ref 18) present a novel fully coupled thermo-mechanical model for FSW, accurately predicting material deformations and temperature fields. Their study explains the correlations between deformation, temperature, microstructure, and texture, highlighting asymmetries in temperature distribution and material flow behavior across thicknesses, thereby informing optimization strategies. They observed a negative impact of TRS on weld joint formation in 6061-T6 aluminum alloy. Huang et al. (Ref 19) studied the joint formation mechanism at constant rotational velocity in FSW Al-Mg-Si alloys through a combined numerical-experimental approach, focusing on high depth-to-width ratio welds using CFD, CSM, and FSI methods. The effectiveness of the proposed numerical model in analyzing joint formation during FSW, especially suited for high depth-to-width ratio welds. Ajri et al. (Ref 20) investigate tunnel and cavity defects in FSW of Al 6061 T6 alloy using experimental and numerical methods, employing a coupled Eulerian-Lagrangian finite element model to analyze the process and optimize parameters. Their study describes the influence of material flow, temperature, and tool action on defect formation. The cavity formation in the top half and tunnel defects in the bottom half of the advancing side (AS) of the weld joint, with cavities prevalent at higher TRS. Xie et al. (Ref 21) introduces a process simulation strategy using numerical models to predict tensile strength in FSW AA2195-T8, validated against experimental data, ensuring its accuracy and rationality. This comprehensive model integrates various numerical techniques including CFD, modified KWN, DRX and recovery, and CSM models, promising essential datasets for further analysis. Moreover, Xie et al. (Ref 22) also develop a thorough process simulation strategy leveraging neural networks to map macro- and microstructural responses of Al-Cu-Li alloys, validating its effectiveness with experimental data. The approach, integrating nested neural networks trained on CFD and microstructural evolution models, elucidates structure-parameter-property relationships, with broad potential application across FSW techniques and materials beyond AA2195 alloy. Pandian and Kannan (Ref 23) study temperature distribution and grain size effects on dissimilar friction stir welded aerospace-grade aluminum alloys 7075 and 2014. Their 3D integrated Multi-physics model, validated through experiments, enhances comprehension of dissimilar alloy welding processes, offering insights for temperature control, grain refinement, and mechanical property enhancement. They observed moderate TRS speeds to improve weld joint mechanical properties. Moradi et al. (Ref 24) analyze welding variable effects on temperature distribution and weld characteristics in friction stir welding of AA5083-O and AA6061-T6 aluminum alloys using finite element modeling and the Johnson-Cook plasticity model.

Their study reveals how TRS, traverse speed, and tool diameter influence temperature distribution and weld geometry, offering insights for optimizing parameters and improving joint quality and efficiency. Results indicate reduced material displacement within the weld area at 740 rpm compared to higher TRS such as 940, 1040, and 1140 rpm.

While previous studies have explored the influence of tool rotation speed (TRS) on material flow velocity and mechanical properties in FSW, there remains a gap in understanding the underlying mechanisms leading to the observed changes in weld quality beyond the optimal TRS point. Specifically, the decrement in mechanical properties after reaching the optimum rotation speed has not been extensively discussed. Although experimental studies have provided valuable insights into the effects of TRS on weld quality, there is a gap in the literature regarding comprehensive numerical analyses that can elucidate the complex interactions between TRS, material flow velocity, and slip rates. A more thorough numerical investigation is necessary to complement experimental findings of mechanical properties and provide a deeper understanding of the underlying processes governing weld quality in FSW. Thus, this article presents a numerical method to predict the TRS for optimum mechanical properties of dissimilar material weld joint of FSW through the temperature and material flow analysis. For this purpose, the computational fluid dynamics (CFD) numerical modeling technique, specifically the Volume of Fluid (VOF) method, is employed to develop a numerical model for FSW of AA5081-H12 and AA6061-T6 aluminum alloys. The model's validity is established by comparing numerical and experimentally calculated temperature profiles. To predict the TRS for optimum mechanical properties, temperature and material flow numerical model is simulated at five different TRS and constant welding speed. The temperature strain rate and material flow are analyzed perpendicular to the weld joint and tool and workpiece interface in AS and RS. Moreover, the slip rate is determined at the interaction between the tool and workpiece materials. The simulation results provide insights into the effect of temperature, strain rate, variations in material flow, and slip rate impact the creation of weld joints and influence their mechanical properties.

2. Experimental Method

The workpiece material used in this study was 5083-H12 (0.02 Si, 0.26 Fe, 0.06 Cu, 0.74 Mn, 4.5 Mg, 0.08 Cr, 0.01 Zn, 0.01 Ti, and balance Al) and AA6061-T6 (0.58 Si, 0.54 Fe, 0.19 Cu, 0.09 Mn, 0.83 Mg, 0.04 Cr, 0.15 Zn, 0.17 Ti, and balance Al) (Ref 25). The workpiece dimensions are 150 mm in length, 50 mm in width, and 6 mm in thickness. In the welding process, 5083-H12 placed in AS and 6061-T6 in RS, respectively (Ref 26-28). The mechanical properties of the 5083-H12 and AA6061-T6 aluminum alloy are given in Table 1. The butt joint welding is carried out using a vertical milling machine (HMT FN2H, 7.5 HP motor capacity). The tool material used was high-carbon steel, and it had a taper cylindrical shape. Taper cylindrical shape tool geometry generates lower welding force and spindle torque while concentrating more heat around the tool pin. This configuration leads to higher material flow velocity, thereby facilitating defect-free welds compared to a cylindrical pin (Ref 29, 30). Additionally, dimensions of the tool, including shoulder

diameter, pin diameter, and pin length, are taken based on literature (Ref 31-33).

Table 2 provides the input process parameters and tool dimensions. The welding input process parameters are selected based on the trial run. To measure the temperature during the welding process, K-type thermocouples are placed 15 mm away from the welding line and 3 mm from the top of the workpiece on both AS and RS. These thermocouples are connected to a data acquisition system for temperature recording. Afterward, to analysis the weld zone shape, the samples are cut in the transverse cross section of the weld joint, polished using different grades of emery paper (from 400 to 2000), and finally etched with a solution consisting of 94 ml distilled water, 3 ml nitric acid, 2 ml hydrochloric acid, and 1 ml hydrofluoric acid (Ref 35, 36). The samples are deep into the etched solution for 40 seconds. A total of 15 samples, 3 per conditions tensile test samples are prepared according to the ASTM E8 M standard and tested at room temperature using an Instron, UK, 8801 universal testing machines (UTM) with a capacity of 50 KN and a crosshead speed of 1 mm/min. The average value of the 3 samples of each condition is taken in the result analysis. Moreover, the fracture surface behaviors are analyzed using a Field Emission Scanning Electron Microscope (FESEM) with the model number Jeol, Japan, JSM-6390LV.

3. Modeling

The heat transfer and material flow simulation of FSW was performed utilizing ANSYS 14.5 software within the framework of computational fluid dynamics (CFD). The placing of material in AS and RS, dimensions of the workpiece, tool, and input process parameter are same as the experimental. During the simulation, it was assumed that the tool's shoulder would enter the workpiece, penetrating it by 0.1 mm starting from the top surface, with the tool itself considered as a rigid body and the workpiece as a fluid. The plasticized material surrounding the rotating tool was treated as a viscous plastic, non-Newtonian, and incompressible medium. The welding is conducted in the X-direction, while the tool rotation occurs in the Z-direction. To analyze the material flow in the weld zone,

the volume of fluid (VOF) method was employed during the simulation.

3.1 Material Properties

In the simulation process, temperature-dependent mechanical properties of the workpiece are used. The specific heat and thermal conductivity of the 5083-H12 and 6061-T6 function of temperature are given in Eq 1-4 (Ref 37, 38).

$$K_{(5083-H12)} = 5.9960 + 1.0117T^1 - 1.7371 \times 10^{-3}T^2 + 1.0288 \times 10^{-6}T^3 \quad (\text{Eq 1})$$

$$C_{(5083-H12)} = 945.52 - 0.4894T^1 + 1.7462 \times 10^{-3}T^2 - 8.9778 \times 10^{-7}T^3 \quad (\text{Eq 2})$$

$$K_{(6061-T6)} = 25.22 + 3.978 \times 10^{-1}T^1 + 7.358 \times 10^{-6}T^2 - 2.518 \times 10^{-7}T^3 \quad (\text{Eq 3})$$

$$C_{(6061-T6)} = 929.3 - 6.270 \times 10^{-1}T^1 + 1.481 \times 10^{-3}T^2 - 4.330 \times 10^{-8}T^3 \quad (\text{Eq 4})$$

Where K, C, and T are the thermal conductivity, specific heat, and temperature. The viscosity (μ) of the materials is the ratio of the effective stress (σ_R) divided by three times the strain rate ($\dot{\epsilon}$) as given in Eq 5 (Ref 39, 40).

$$\mu = \frac{\sigma_R}{3\dot{\epsilon}} \quad (\text{Eq 5})$$

The effective stress (σ_R) and Zener-Holloman parameter (Z) is calculated by eq 6 and 7. The material properties parameters values of 5083-H12 and 6061-T6 are given in Table 3.

$$\sigma_R = \frac{1}{\alpha} \ln \left[\left(\frac{Z}{A} \right)^{\frac{1}{n}} + \left(1 + \left(\frac{Z}{A} \right)^{\frac{2}{n}} \right) \right]^{\frac{1}{2}} \quad (\text{Eq 6})$$

$$Z = \dot{\epsilon} \exp \left(\frac{Q}{RT} \right) \quad (\text{Eq 7})$$

Table 1 Mechanical properties of the workpiece materials (Ref 34)

Alloys	Yield stress, Mpa	Ultimate Strength, Mpa	% Elongation
6061-T6	275.90	301.20	10.12
5083-H12	411.42	438.19	6.72

Table 2 Welding input parameters and tool dimensions

Welding parameters	Unit	Values
Welding speed (Ref 33)	mm/min	63
TRS	rpm	710,900,1120, 1400, and 1600
Tool shoulder diameter	mm	18
Pin diameter (top and bottom)	mm	6 to 4
Pin length	mm	5.7

Table 3 Material properties parameters (Ref 41–43)

Parameters	6061-T6	5083-H12
Q (kJ/mol), activation energy,	145	171
α , material constant	0.03E-6	0.019E-6
A (S ⁻¹), material constant	2.4E8	1.09E10
n, material constant	3.55	4.99
Density (kg/m ³)	2700	2660
Solidus temperature (K)	855	843

3.2 VOF Method

The volume of fluid (VOF) method is used in the numerical model to simulate dissimilar FSW weld joints. The VOF method helps to analyze the phase distribution of the dissimilar materials of the FSW weld joint. The numerical modeling of the dissimilar FSW weld joint with different physical properties of the material is based on the continuity, momentum, and energy conservation that are given in eq 8, 9, and 10, respectively. The amount of mixing of the material in the weld nugget zone (WNZ) of dissimilar FSW of weld joint is determined by volume fraction (β). The primary and secondary phases are 6061-T6 and 5083-H12, respectively. The volume fraction of the primary (β_p) and secondary phases (β_s) lies between 0 to 1. The zero indicates that no amount of fluid material is present in the phases, and one means the phases are full of fluid materials; as a result, the sum of the β is always unity.

$$\frac{\partial}{\partial t}(\beta_A \rho_A) + \nabla \cdot (\beta_A \rho_A \vec{v}) = 0 \quad (\text{Eq 8})$$

$$\begin{aligned} \frac{\partial}{\partial t}(\beta_A \rho_A \vec{v}) + \nabla \cdot (\beta_A \rho_A \vec{v} \vec{v}) &= \vec{F} - \nabla P \\ &+ \nabla \cdot [\mu_A (\beta_A (\nabla \vec{v} + \nabla \vec{v}^T))] + \beta_A \rho_A \vec{g} \end{aligned} \quad (\text{Eq 9})$$

$$\rho_A C_A \left(\frac{\partial T}{\partial t} + \vec{v} \cdot \nabla T \right) = \nabla \cdot K_A (\nabla T) \quad (\text{Eq 10})$$

Where, P, K, C, T, ρ , and \vec{v} are the pressure, thermal conductivity, specific heat, density, temperature, and material flow velocity vector of the workpiece material, respectively.

3.3 Boundary Conditions

The material position, tool rotation, and welding direction in the numerical model are shown in Fig. 1(a). The numerical model generates heat at the interface between the tool and workpiece based on partial sticking and sliding conditions.

The three interface surfaces, which are tool shoulder (TS), pin side (TPS), and pin bottom (TPB) surfaces are responsible for heat generation in the welding process as shown in Fig. 1(b). The heat generated at the interface is calculated and divided by the surface area of the respective surfaces to find the heat flux value. The TS, TPS, and TPB heat flux are calculated based on eq 11–13, respectively. Afterward, the calculated heat flux value of each surface is given to the manually created interface of the tool and workpiece of the respective surface.

$$q_{TS} = \frac{[\delta_{TS} \tau_b + (1 - \delta_{TS}) \mu P] \bullet 2\omega(R_1^2 + R_2^2 + R_1 R_1)}{3(R_1 + R_2)} \quad (\text{Eq 11})$$

$$q_{TPS} = \frac{2\delta_{TPS} \omega \tau_b (R_2^3 - R_3^3) \cos \varphi}{3(R_2^2 - R_3^2)} + \frac{2(1 - \delta_{TPS}) \mu \omega P_1 (R_2^3 - R_3^3)}{3(R_2^2 - R_3^2)} \quad (\text{Eq 12})$$

$$q_{TPB} = \frac{2}{3} \omega R_3 \delta_{TPB} \tau_b + (1 - \delta_{TPB}) \mu P \quad (\text{Eq 13})$$

Where δ is the contact state variable, and its value lies between 0 and 1 (Ref 44). τ_b , ω , and P are the shear stress, viscosity, TRS, and pressure. The R_1 , R_2 and R_3 are the radius of the tool shoulder, pin top, and bottom surface, respectively. The conduction heat transfer conditions are provided to the workpiece's top surface such as 200 W/m²-K and convection in the top surface and sidewall such as 25 W/m²-K (Ref 45). The material properties, heat generation equations, and boundary conduction conditions discussed above are written in the user-define function (UDF). The UDF is a self-written micro code uploaded into ANSYS FLUENT with the help of a user-define option and solved by the FLUENT solver.

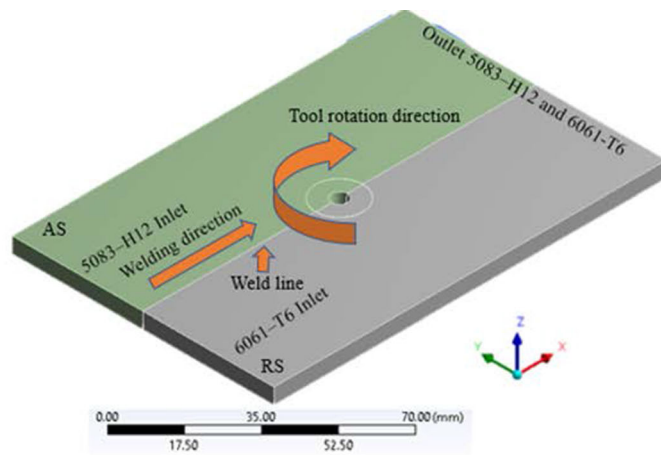
To verify the accuracy of the numerical model the temperature distribution results obtained from simulation and experiment are compared. Figure 2 shows the comparison of simulated peak temperature result with experimental generated peak temperature at a welding condition of 910 rpm and 63 mm/min. In the simulated the temperature profile is taken as the same position that is discussed in the experimental method section. It is observed that the simulated temperature distribution curve closely matches with the experimental temperature distribution curve. The maximum experimental temperatures recorded by the thermocouples in the AS and RS were 555 and 547 K and simulated temperatures were 543 and 534 K, respectively. Similar trends are observed for other tool rotation speeds and indicate that the difference between the simulated and experimental peak temperatures in AS and RS is approximately 3%.

4. Results and Discussion

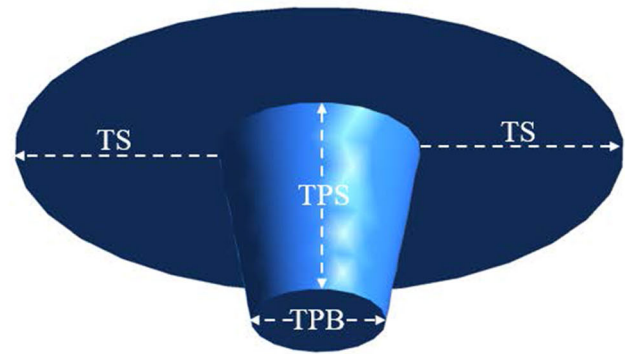
4.1 Effect of TRS on Temperature Generation

Figure 3(a), (b), (c), (d), and (e) shows the temperature distribution profile of the perpendicular to the weld joint at different TRS of 710, 900, 1120, 1400, and 1600 rpm. The peak temperature increases with increasing the TRS. The amount of friction heat between the tool and workpiece increases with increasing the TRS and thus increasing the peak temperature in the weld joint (Ref 46).

This temperature distribution is attributed to the stirring effect of the shoulder, which generates significant heat. This heat is then dissipated toward the bottom and the surrounding wall, resulting in the observed temperature contour. The contour is wider near to the shoulder and becomes narrower toward the bottom. Additionally, the temperature distribution contour in RS is slightly lower compared to the AS, indicating

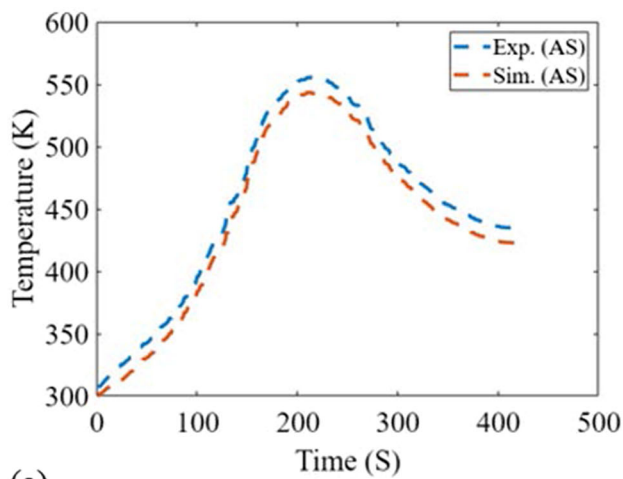


(a)

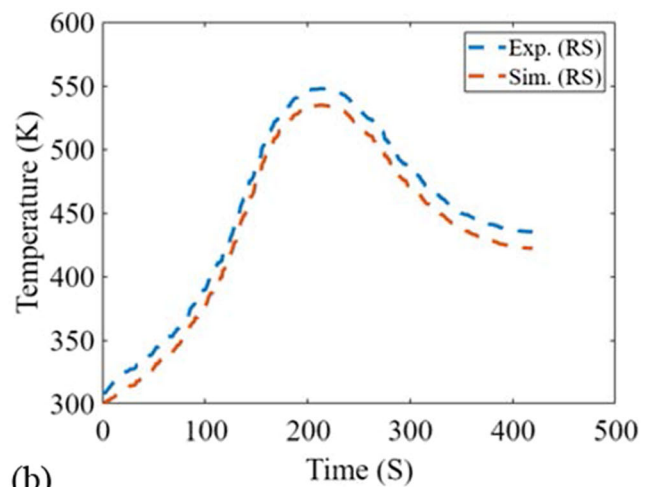


(b)

Fig. 1 Simulation boundary conditions



(a)



(b)

Fig. 2 Experimental and simulation temperature distribution at 900 rpm and 63 welding speed (a) AS and (b) RS

an asymmetric temperature distribution between both sides as shown in Fig. 3(a), (b), (c), (d), and (e). This asymmetry arises due to the workpiece material placed on RS having slightly higher thermal conductivity, leading to greater heat loss compared to workpiece material placed on AS. The simulated peak temperature top and bottom in AS and RS at different TRS are given in Table 4. And the differences between these peak temperatures and the solidus temperatures of AA6061-T6 and 5083-H12 in terms of the ratio are calculated and given in Table 3. Ajri et al. (Ref 20) and Selvaraj et al. (Ref 47) explain that for the 70 to 90 % solidus temperature (approximately 598 to 770 K in case of 6061-T6) of the workpiece material is required for adequate material flow from RS to AS to develop defect-free weld joint.

Upon analysis of Table 4, it becomes evident that, at TRS values of 900, 1120, and 1400 rpm, the temperature range in RS, spanning from the top to the bottom of the workpiece, falls within the critical 70% to 90% range. However, at TRS values of 710 and 1600 rpm, the temperature range in RS deviates below and above the 70% to 90% range, respectively. Additionally, Fig. 3(f) shows the strain rate distribution perpendicular to the weld joint at different TRS. The relation-

ship between TRS and strain rate is readily observable, as an increase in TRS leads to a rise in strain rate. The evident observation is that the strain is more pronounced on top surface when compared to bottom surface. This discrepancy is attributed to the significant role played by the rotating tool shoulder in driving material deformation, surpassing the contribution of the tool pin. Moreover, the strain rate in AS of the welding is lower as compared to the RS. This asymmetric nature is due to the material placed in RS 6061-T6 having lower activation energy compared to 5083-H12 placed in AS. It means that the material 6061-T6 required less energy to activate dislocations and initiate plastic deformation compared to 5083-H12. Similar observations have been reported by Gotawala and Shrivastava (Ref 48) in FSW of copper and AA 1050. The fluctuation in temperature and strain rate due to varying TRS has a substantial impact on several key aspects, including material flow velocity, the conduction of contact between the tool and workpiece, and ultimately, the formation of the weld zone and mechanical properties of the weld joint as examined in the following section.

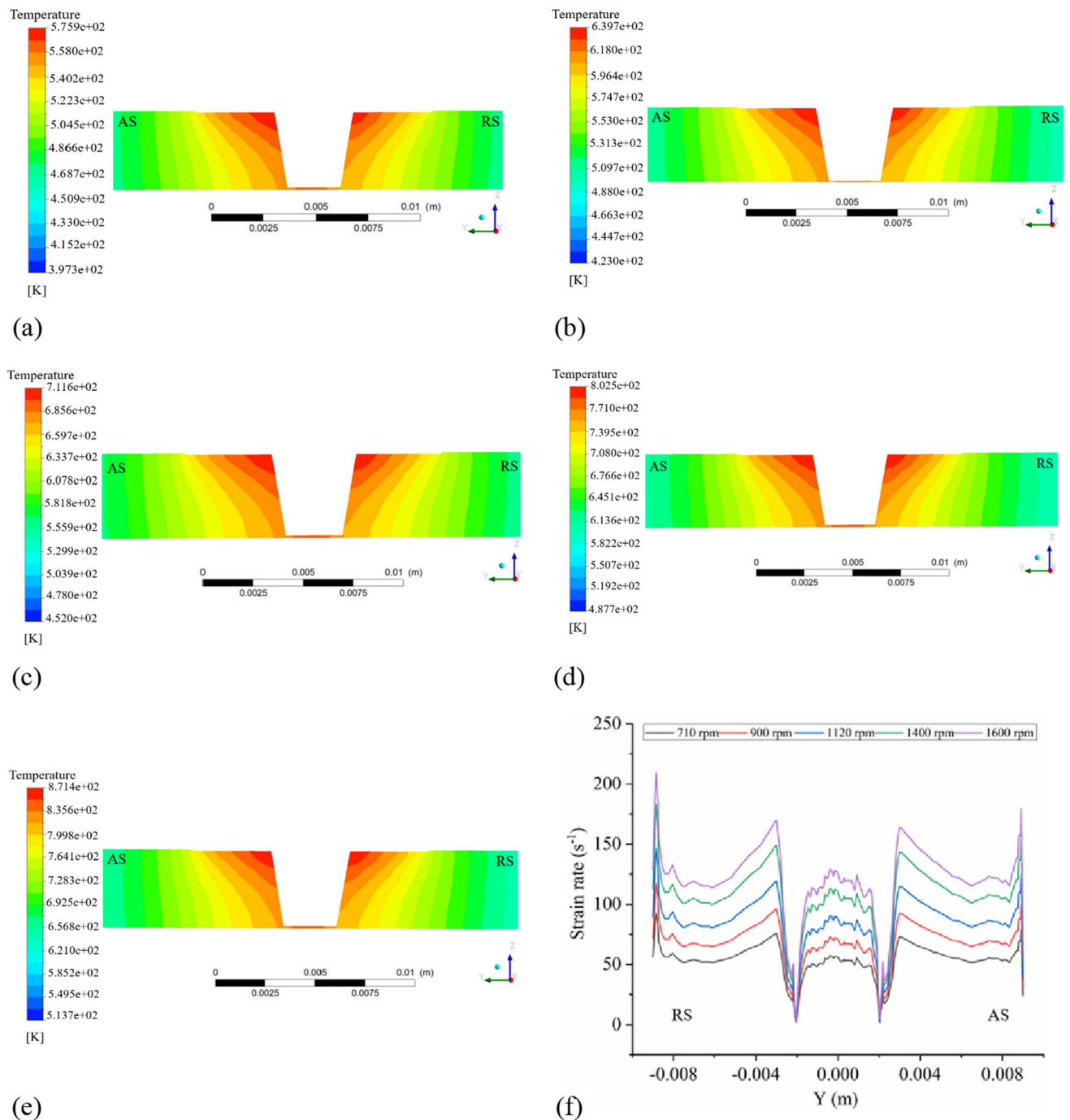


Fig. 3 Temperature distribution perpendicular to the weld joint (a) 710, (b) 900, (c) 1120, (d) 1400 and (e)1600 rpm and (f) strain rate distribution perpendicular to the weld joint in all TRS

Table 4 Simulated peak temperature at different TRS

Simulated peak temperature, K	710		900		1120		1400		1600	
	AS	RS	AS	RS	AS	RS	AS	RS	AS	RS
Top	575	573	639	637	711	710	802	801	871	870
bottom	552	547	611	606	677	672	760	775	821	815
T/T _{solidus} (Top) %	68	67	75	74	84	83	95	93	103	101
T/T _{solidus} (Bottom) %	65	63	72	70	80	78	90	88	97	95

4.2 Effect of TRS on Material Flow Velocity

The material flow velocity contours of the perpendicular to the weld joint cross section are shown at 710, 900, 1120 and 1400, rpm and 1600 rpm TRS shown in Fig. 4. The material moves in a negative Y direction representing RS and in a positive Y direction for AS, respectively, as shown in Fig. 4(a). The velocity of material flow is higher at the top of the workpiece and gradually decreases along the depth of the workpiece in all TRS, as shown in Fig. 4(b), (c), (d), and (e).

This is because the stirring effect of the tool shoulder is more pronounced at the top of the workpiece and reduces along the depth. The contour lines of material flow velocity follow the same pattern in all TRS. However, the variations of the magnitude of the material flow in the weld zone are observed with variation in TRS. The peak material flow velocity at the top surface of the workpiece is slightly higher in the RS compared to the AS. As previously explored in the above section, the higher strain rate observed in the RS implies a correspondingly greater material flow velocity when compared to the AS. This relationship is established by the direct proportionality between strain rate and material flow velocity (Ref 49). All the material flow velocity contour lines first, second, and third which are near to the shoulder show that material flow velocity increases with increasing the tool rotation speed from 700 to 1600 rpm, but the last three contour lines show that material flow velocity increases with increasing the TRS up to 1120 rpm and material flow velocity decreases on further increasing the TRS. The alteration of the material

flow velocities of the contour lines can be used to determine the optimum material flow by numerical analysis. To investigate the reason of alternation of material flow velocities of the contour lines, material flow velocities at interface of the tool and workpiece is determined because material flow velocity start at interface and produces the contour of material flow velocity in the weld zone.

Material flow velocity along the tool and workpiece interface at different TRS, six different points in RS and AS are taken, as shown in Fig. 5(a). The material flow velocity in AS and RS at the interface is compared at all TRS are shown in Fig. 5(b), (c), (d), (e), and (f). The horizontal axis represents the distance from center of tool pin to shoulder from bottom to top of the workpiece. Figure 5(b) shows that at a lower TRS of 710 rpm, the material flow velocity in RS at the bottom of the interface of tool and workpiece in RS is slightly lower than AS (point F in RS and 6 in AS). This difference can be attributed to the insufficient temperature generated at the bottom of the workpiece in RS, which fails to facilitate the plastic deformation of materials stirred from RS to AS. Consequently, the material flow velocity in RS at the bottom of the interface of tool and workpiece is reduced. Increasing the TRS 900, 1120, and 1400 rpm the temperature at the bottom of the interface of tool and workpiece increases. Therefore, stirring of plastic deformation of materials from RS to AS increases. The material flow velocity in RS is 14, 16, 8% higher than the AS at above the bottom of the workpiece. The material flow velocity in both AS and RS exhibit similar trends at 700, 900, and 1120 rpm.

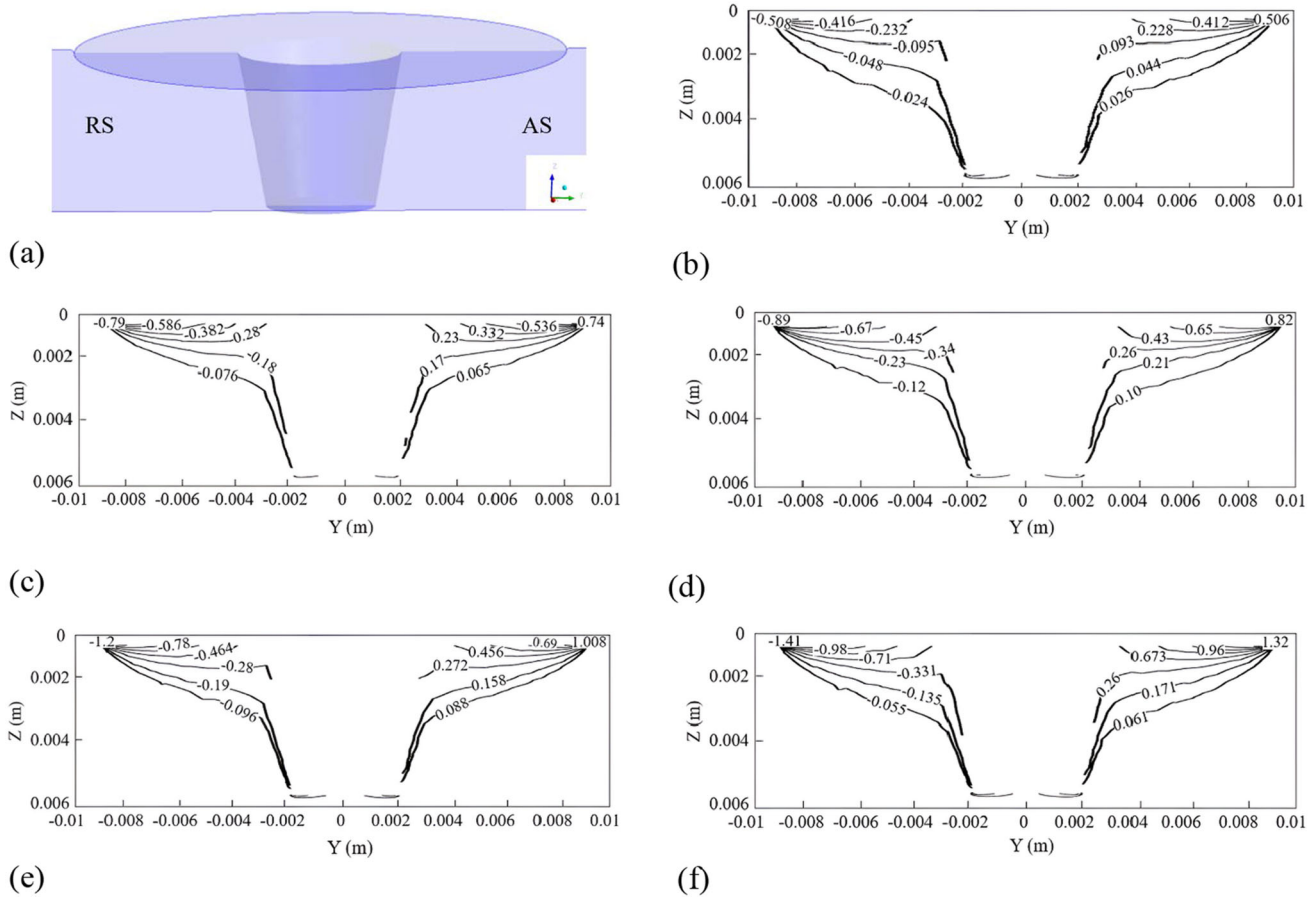


Fig. 4 (a) Direction of material flow and material flow velocity at (b) 710 rpm, (c) 900 rpm, (d) 1120 rpm, (e) 1400 rpm, and (f) 1600 rpm

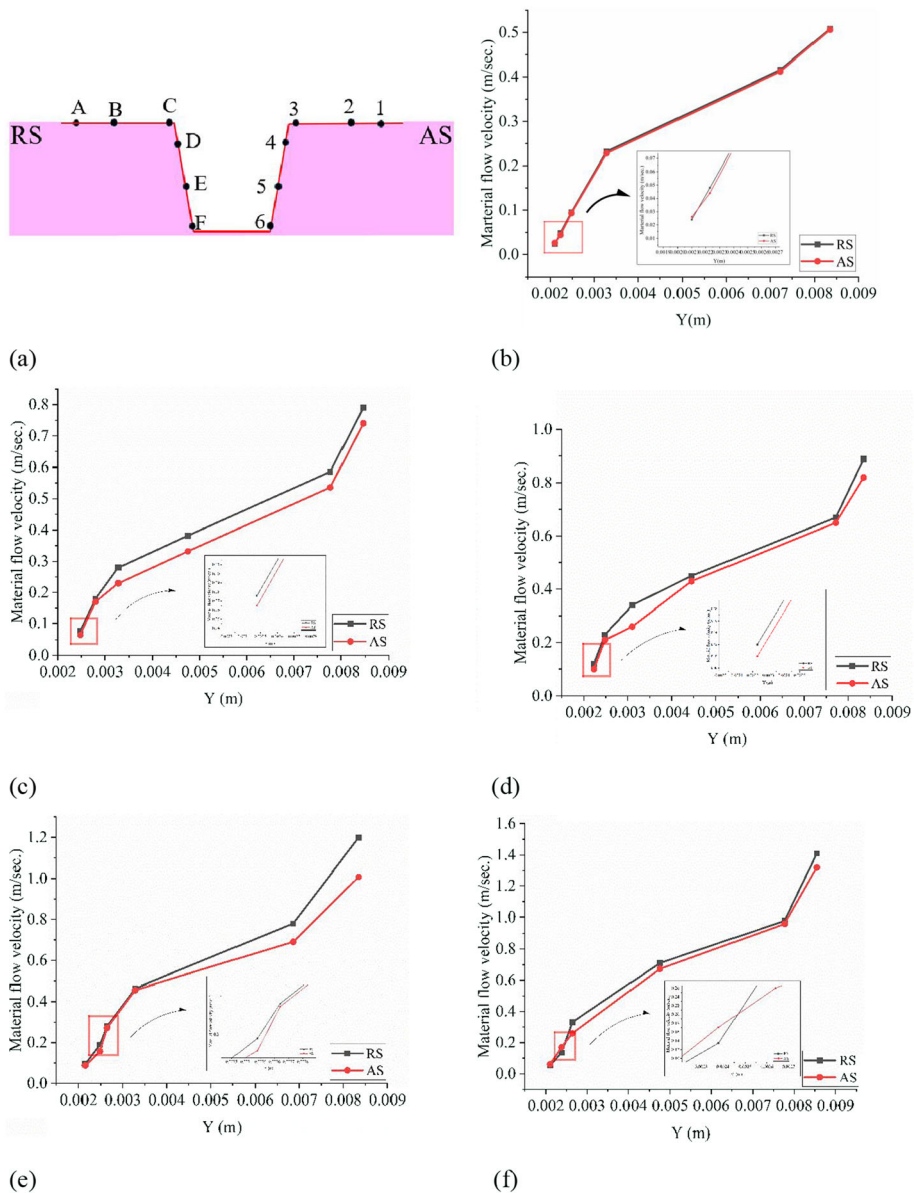


Fig. 5 Variation in material flow velocity along the depth of workpiece in AS and RS at different TRS (a) 710, (b) 900 (c) 1120 (d) 1400, and (e) 1600 rpm

However, at 1400 and 1600 rpm the magnitude of the material flow velocity at the bottom of the interface of tool and workpiece decreases and its magnitude lies between 900 and 1120 rpm. Moreover, at 1600 rpm the material flow velocity in RS (point E, F) is lower than AS (point 5, 6) in the bottom of the interface of tool and workpiece. The results of the study reveal that at high TRS values, the magnitude of material flow in the RS is reduced near the bottom due to generation of higher temperature that result in accumulation of material. At 1400 rpm the temperature generates in RS above the bottom of the workpiece (point E, F) is approximately 90 % of the solidus temperature of the workpiece material. Thus, the accumulation of material started at the bottom of the workpiece that result in the decreasing the magnitude of the material flow velocity. However, at 1600 rpm the temperature generates in

RS above the bottom of the workpiece (point E and F) is more than 95 % of the solidus temperature of the workpiece material. It means that, the higher accumulation of material and excessive turbulence in the plasticized deform material that reduces the material flow velocity in RS. The accumulation of the material in RS above the bottom of the workpiece at higher TRS 1400, 1600 rpm and insufficient stirring of the material at lower TRS 710 rpm which means that the contact condition at the tool and workpiece interface specially at the bottom of the workpiece are not uniform. The contact condition at the tool and workpiece interface described by the slip rate which is the ratio of material flow velocity to the tool velocity at the respective contact point. The slip rate describes the occurrence of sticking, sliding, and partial sticking and sliding phenomena in the zone where the tool meets the workpiece. When the slip

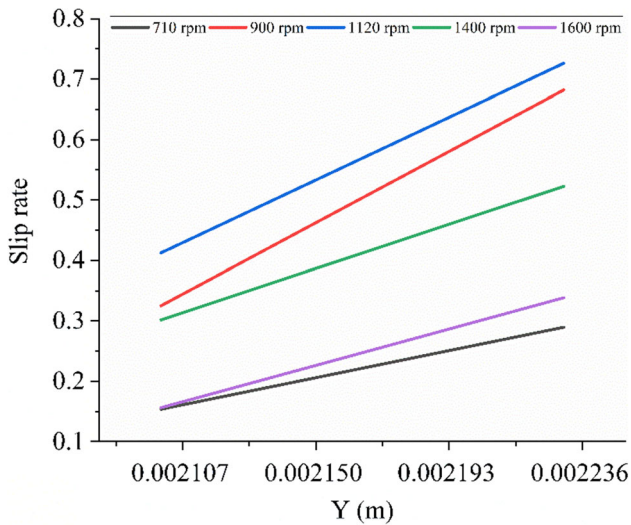


Fig. 6 Variation in the slip rate at point E and F in RS

rate tends toward one, the sticking phenomenon dominates, whereas a slip rate approaching zero indicates a sliding phenomenon (Ref 50, 51). The slip rate at different TRS, especially at the bottom of the workpiece (Point F, E in RS) are shown in Fig. 6.

Increasing the TRS 710 to 1120 rpm the slip rate at point F, E in RS increases and its value decreases with increasing the TRS 1400 to 1600 rpm. The slip rate value at point F on 710, 900, 1120, 1400, and 1600 rpm are 0.156, 0.325, 0.412, 0.301, and 0.156, respectively. The lower slip rate at 710 and 1600 rpm on point F results in more sliding phenomenon dominating as compared to 900, 1120, and 1400 rpm.

This phenomenon highlights the importance of considering material accumulation and its effect on the contact condition of the tool and workpiece interface during the welding process. As it can significantly influence the contact condition between tool and workpiece interface and ultimately affect the quality of the weld joint. The effect of the accumulation of the material develops the nonuniform contact condition between tool and workpiece which finally produces defects and reduces strength weld joint as described in the following section.

4.3 Effect of TRS on Weld Zone

The formation of the weld zone at different TRS is shown in Fig. 7. Defect-free weld joints are achieved at tool rotation speeds of 900, 1120, and 1400 rpm, as shown in Fig. 7(b), (c), and (d). And defects are observed in the weld zone at 710 and 1600 rpm as shown in Fig. 7(a) and (e). This is because of the lower slip rate at 710 and 1600 rpm of the bottom of the tool-workpiece interface. That results in more sliding phenomenon dominating as compared to at the bottom of the workpiece which causes the defect formation in the weld joint. Moreover, it is observed from Fig. 7 the average thickness of intermetallic compounds (IMC) decreases with increasing the TRS 710 to 1120 rpm and further increasing the TRS 1400 to 1600 rpm the

IMC thickness increases as shown in Fig. 7(a), (b), (c), (d), and (e).

The average IMC thickness was 2.7, 2.15, 1.57, 2.62, and 4.1 μm on RS and 2.23, 1.63, 1.35, 2.38, and 2.56 μm on AS at TRS of 710, 900, 1120, 1400, and 1600 rpm, respectively. The variation in the IMC in the weld zone effect due to variation in the temperature, material flow velocity with TRS as discussed in the previous sections. The variation in IMC within the weld area impacts the mechanical characteristics of the welded joint, as discussed in the next section.

4.4 Effect of TRS on Tensile Strength and Fracture Behavior

The fracture location of the tensile samples at different TRS is shown in Fig. 8(a), and the fracture behaviors are analyzed using a Field Emission Scanning Electron Microscope (FESEM) as shown in Fig. 8(b), (c), (d), (e), and (f). The weld joint's tensile strength varies with different TRS at 710, 900, 1120, 1400, and 1600 rpm, the strengths are 150, 163, 176, 142, and 135 MPa, respectively. As the TRS increases from 710 to 1120 rpm, the tensile strength of the weld joint also increases. However, at higher TRS 1400 and 1600 rpm, the tensile strength decreases. The optimal tensile strength is observed at 1120 rpm and a speed of 63 mm/min. This is because at this welding condition the lower average thickness of the IMC in RS and AS is observed as compared to another weld joint. The fracture occurred at the weld nugget zone in all weld joint. However, at the optimum welding conditions the fracture path is inclined to the tensile loading direction.

The fracture surface shows that the appearance of the voids and dimples with different shape and size increases with increasing the TRS 710 to 1120 rpm as shown in Fig. 8(b), (c), and (d). This indicates material suffers massive plastic deformation and requires high energy prior to the fracture occurrence and shows ductile fracture behavior. However, increasing the TRS 1400 rpm smaller dimples are presents in the fracture surface. As a result, inductile and brittle fracture behavior as shown in Fig. 8(e).

Further, increasing the TRS 1600 rpm formation of flat surface is observed at the fracture surface it suggests that the fracture occurred with minimal deformation and rapid propagation of cracks and indicates material experienced a sudden failure, characteristic of brittle behavior (Ref 52). It is also observed that the necking phenomenon is observed at the fracture surface of the weld joint developed at 1120 rpm and 63 mm/min as shown in Fig. 8(a) and (d). This means that the more ductile fracture behavior as compared to the other weld joint.

5. Conclusions

The numerical analysis of the dissimilar material weld joint using Friction Stir Welding (FSW) has provided valuable insights into the effect of TRS on the weld joint formation and mechanical properties. The following conclusions can be drawn from the study:

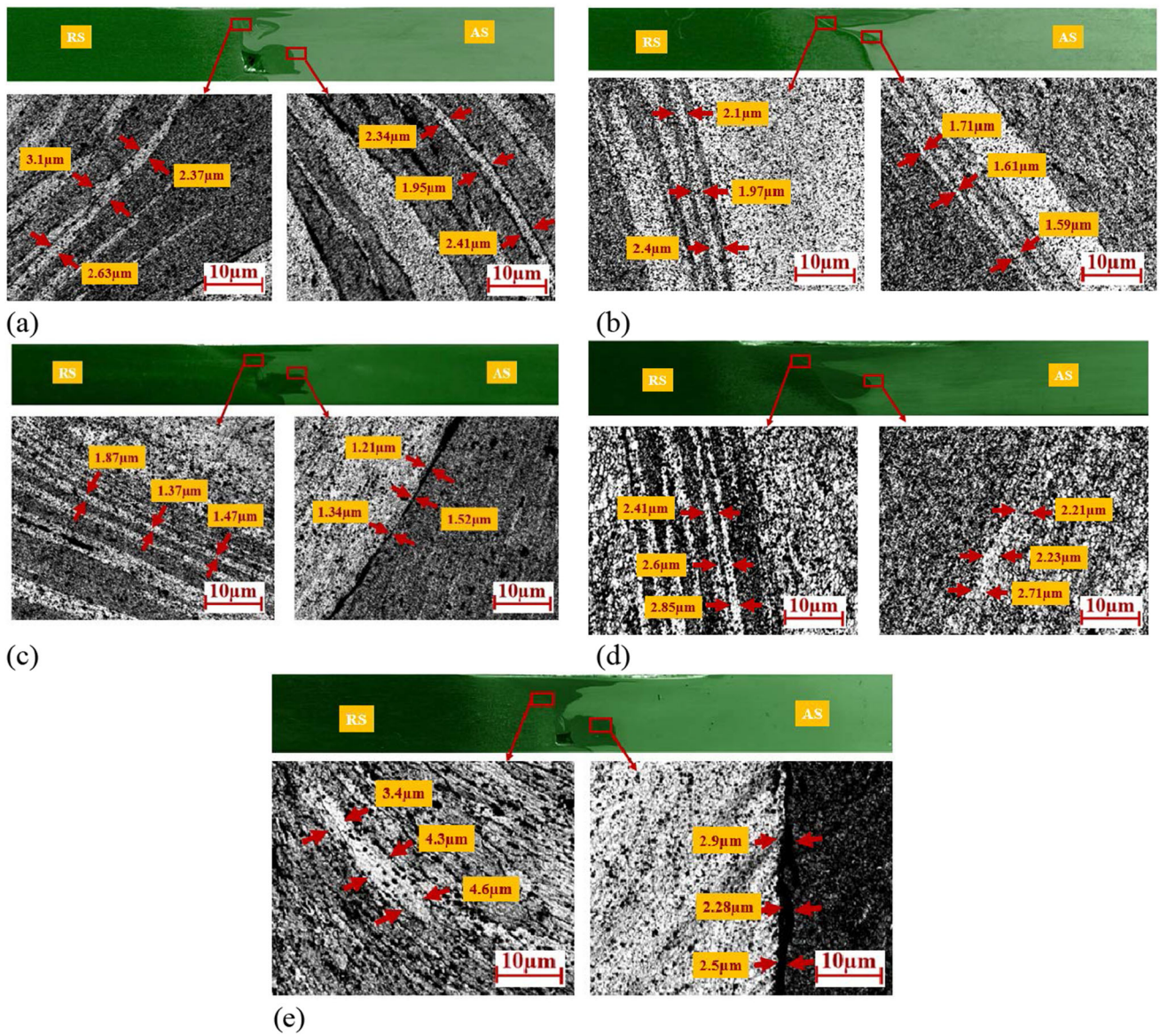


Fig. 7 Microstructure at the interface of SZ and TMAZ (a) 710 rpm (b) 900 rpm (c) 1120 rpm (d) 1400 rpm, and (e) 1600 rpm

- Optimizing tool rotation speed (TRS) is essential for precise temperature control during welding. At TRS values of 710 and 1600 rpm, temperatures deviate below and above the critical range of 70 to 90%, solidus temperature of the workpiece which producing the defect in the weld joint. Maintaining TRS within this range is vital for ensuring consistent and high-quality welds as obtained defect-free joint at 900, 1120, and 1400 rpm.
- Material flow velocity at the tool-workpiece interface follows the same trend at 710, 900, and 1120 rpm, but the trend shifts after reaching 1120 rpm near the bottom of the tool-workpiece interface affecting weld quality.
- Slip rates signify the transition from sticking to sliding phenomena, impacting weld quality. Slip rates increase initially with tool rotation speed from 710 to 1120 rpm near the bottom of the weld but decrease thereafter. Lower slip rates at 1400 and 1600 rpm indicate increased sliding, potentially leading to decreased tensile strength and formation of defects in weld joints.

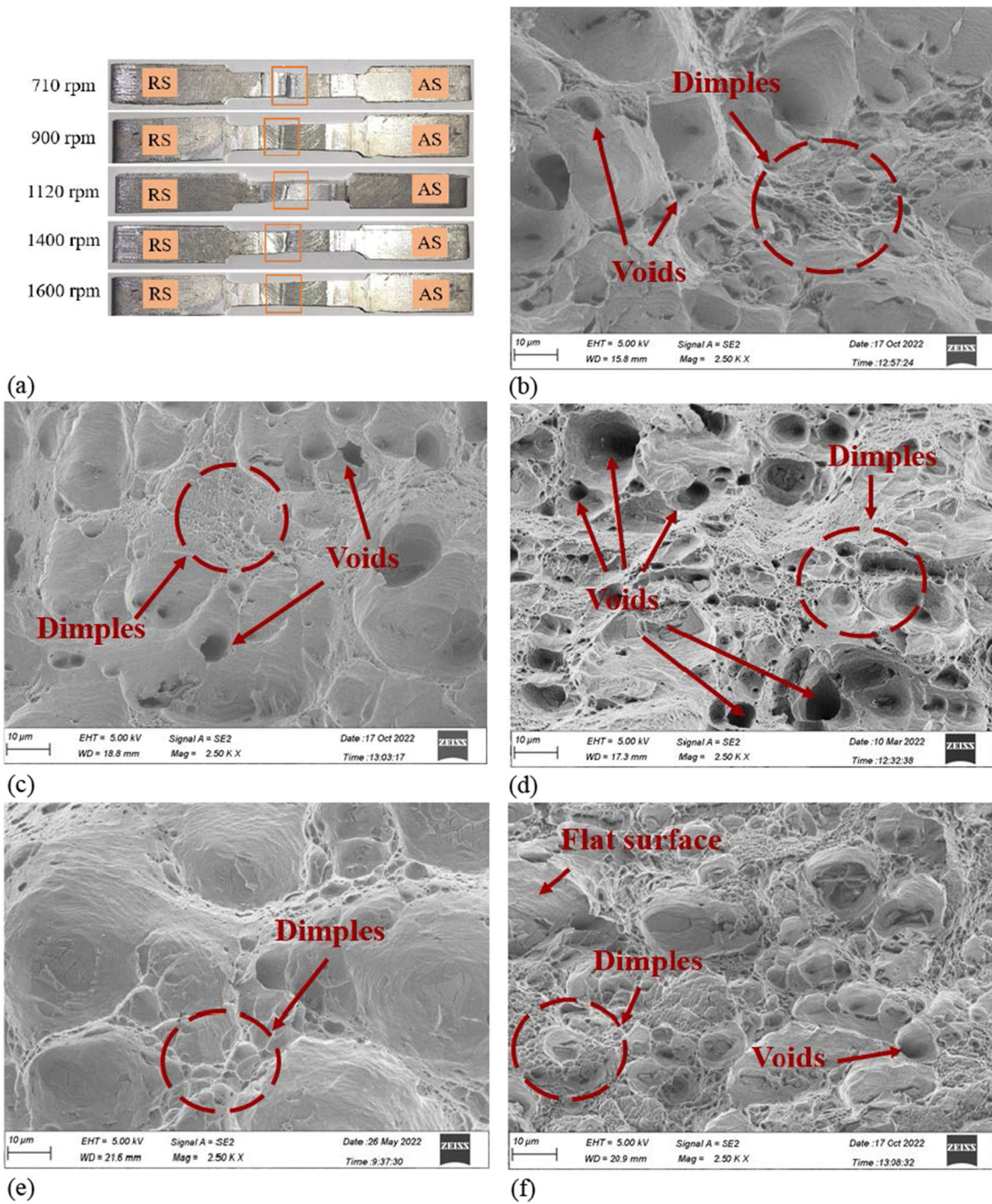


Fig. 8 (a) Fracture location at different TRS. FESM fractures image of the weld joint (b) 700, (c) 900, (d) 1120 and (e) 1400 (f) 1600 rpm

- Defect-free weld joints are attained at 900, 1120, and 1400 rpm, with observed defects occurring at 710 and 1600 rpm. The optimal tensile strength of 174 MPa is associated with lower intermetallic compound thickness at 1120 rpm, while achieving improved ductile fracture mode compared to all weld joints.

These findings highlight the importance of TRS in influencing temperature distribution, material flow velocity, weld joint formation, and mechanical properties in dissimilar material weld joints. Numerical analysis provides a valuable tool for predicting the optimal tool rotation speed and optimizing the

FSW process to achieve defect-free weld joints with desirable mechanical properties.

Acknowledgment

The authors thank Central Instrumentation Facility (CIF) Lab, BIT, Mesra, Ranchi for providing the research facilities of material testing.

References

1. A. Mangain, V. Singh, and A. Pratap Singh, Influence of Welding parameters on Mechanical property during Friction Stir Welded joint on Aluminium Alloys: A Review, *J. Kejuruter.*, 2023, **35**(1), p 13–28
2. U. Acharya, U. Kumar, M. Ghosh, S. Choudhury, A.K. Srivastava, and B.S. Roy, An Experimental Approach for Achieving High Strength Dissimilar Aluminium-magnesium Joints: Application of Tool Pin Profiles on Different Joint Configurations, *CIRP J. Manuf. Sci. Technol.*, 2023, **45**, p 49–60
3. K. Singh, G. Singh, and H. Singh, The Influence of Holding Time on the Characteristics of Friction Stir Welded Dissimilar Magnesium Alloy Joints During Post Welding Heat Treatment, *Proc. Inst. Mech. Eng. Part L J. Mater. Des. Appl.*, 2023, **237**(1), p 170–182
4. M.M. Ahmed, M.M. El-Sayed Seleman, D. Fydrych, and G. Çam, Friction Stir Welding of Aluminum in the Aerospace Industry: The Current Progress and State-of-the-Art Review, *Materials*, 2023, **16**(8), p 2971
5. A. Rabieezadeh, A. Salafzon, and N. Mostafavi, Dissimilar Welding of AA5083/AA7039 by Self-reacting Friction Stir Welding, *J. Adhes. Sci. Technol. Adhes. Sci. Technol.*, 2023, **38**, p 1–22
6. S. Meng, H. Liu, J. Xiao, T. Huang, Y. Ni, and S. Sun, A Method for Process Parameter Optimization of Simultaneous Double-sided Friction Stir Welding Using a Heat Transfer Model, *Int. J. Adv. Manuf. Technol.*, 2022, **121**(5–6), p 3747–3758
7. A.H. Baghdadi, A. Rajabi, N.F. Selamat, Z. Sajuri, and M.Z. Omar, Effect of Post-weld Heat Treatment on the Mechanical Behavior and Dislocation Density of Friction Stir Welded Al6061, *Mater. Sci. Eng. A*, 2019, **29**(754), p 728–734
8. X. Meng, Y. Huang, J. Cao, J. Shen, and J.F. dos Santos, Recent Progress on Control Strategies for Inherent Issues in Friction Stir Welding, *Prog. Mater. Sci. Mater. Sci.*, 2021, **115**, p 100706
9. X. Meng, Y. Xie, S. Sun, X. Ma, L. Wan, J. Cao, and Y. Huang, Lightweight Design: Friction-Based Welding Between Metal and Polymer, *Acta Metall. Sin. (English Letters)*, 2023, **36**(6), p 881–898
10. K. Elangovan, V. Balasubramanian, and M. Valliappan, Influences of Tool Pin Profile and Axial Force on the Formation of Friction Stir Processing Zone in AA6061 Aluminium Alloy, *Int. J. Adv. Manuf. Technol.*, 2008, **38**, p 285–295
11. R. Kumar, K. Singh, and S. Pandey, Process Forces and Heat Input as Function of Process Parameters in AA5083 Friction Stir Welds, *Trans. Nonferrous Metals Soci. China*, 2012, **22**(2), p 288–298
12. R. Moshwan, F. Yusof, M.A. Hassan, and S.M. Rahmat, Effect of Tool Rotational Speed on Force Generation, Microstructure and Mechanical Properties of Friction Stir Welded Al-Mg-Cr-Mn (AA 5052-O) Alloy, *Mater. Des. (1980-2015)*, 2015, **5**(66), p 118–128
13. S. Sudhagar, M. Sakthivel, P.J. Mathew, and S.A.A. Daniel, A Multi Criteria Decision Making Approach for Process Improvement in Friction Stir Welding of Aluminium Alloy, *Measurement*, 2017, **108**, p 1–8
14. S. Ahmed and P. Saha, Selection of Optimal Process Parameters and Assessment of Its Effect in Micro-friction Stir Welding of AA6061-T6 Sheets, *Int. J. Adv. Manuf. Technol.*, 2020, **106**(7–8), p 3045–3061
15. R.I. Rodriguez, J.B. Jordon, P.G. Allison, T. Rushing, and L. Garcia, Microstructure and Mechanical Properties of Dissimilar Friction Stir Welding of 6061-to-7050 Aluminum Alloys, *Mater. Des.*, 2015, **15**(83), p 60–65
16. C. Zhang, G. Huang, Y. Cao, Y. Zhu, and Q. Liu, On the Microstructure and Mechanical Properties of Similar and Dissimilar AA7075 and AA2024 Friction Stir Welding Joints: Effect of Rotational Speed, *J. Manuf. Process.*, 2019, **1**(37), p 470–487
17. O.P. Abolusoro, E.T. Akinlabi, and S.V. Kailas, Tool Rotational Speed Impact on Temperature Variations, Mechanical Properties and Microstructure of Friction Stir Welding of Dissimilar High-Strength Aluminium Alloys, *J. Braz. Soc. Mech. Sci. Eng.*, 2020, **42**, p 1–2
18. Z. Zhang and H.W. Zhang, A Fully Coupled Thermo-mechanical Model of Friction Stir Welding, *Int. J. Adv. Manuf. Technol.*, 2008, **37**, p 279–293
19. Y. Huang, Y. Xie, X. Meng, J. Li, and L. Zhou, Joint Formation Mechanism of High Depth-to-width Ratio Friction Stir Welding, *J. Mater. Sci. Technol.*, 2019, **35**(7), p 1261–1269
20. A. Ajri, N. Rohatgi, and Y.C. Shin, Analysis of Defect Formation Mechanisms and their Effects on Weld Strength During Friction Stir Welding of Al 6061-T6 via Experiments and Finite Element Modeling, *Int. J. Adv. Manuf. Technol.*, 2020, **107**, p 4621–4635
21. Y. Xie, X. Meng, and Y. Huang, Entire-process Simulation of Friction Stir Welding—Part 1: Experiments and Simulation, *Weld. J.*, 2022, **5**, p 144
22. Y. Xie, X. Meng, and Y. Huang, Entire-process Simulation of Friction Stir Welding—Part 2: Implementation of Neural Networks, *Weld. J.*, 2022, **101**, p 172–177
23. V. Pandian and S. Kannan, Numerical Prediction and Experimental Investigation of Aerospace-grade Dissimilar Aluminium Alloy by Friction Stir Welding, *J. Manuf. Process.*, 2020, **54**, p 99–108
24. M. Moradi, M.S. Meiabadi, and V. Demers, A Numerical Investigation of Friction Stir Welding Parameters in Joining Dissimilar Aluminium Alloys Using Finite Element Method, *Int. J. Manuf. Res.*, 2021, **16**(1), p 32–51
25. M. Ghaffarpour, A. Aziz, and T.H. Hejazi, Optimization of Friction Stir Welding Parameters Using Multiple Response Surface Methodology, *Proc. Inst. Mech. Eng. Part L J. Mater. Des. Appl.*, 2017, **231**(7), p 571–583
26. N.R. Ramesh and V.S. Kumar, Experimental Erosion-Corrosion Analysis of Friction Stir Welding of AA 5083 and AA 6061 for Sub-sea Applications, *Appl. Ocean Res.*, 2020, **98**, p 102121
27. V.R. Kishore, J. Arun, R. Padmanabhan, and V. Balasubramanian, Parametric Studies of Dissimilar Friction Stir Welding Using Computational Fluid Dynamics Simulation, *Int. J. Adv. Manuf. Technol.*, 2015, **80**(1), p 91–98
28. S. Verma and J.P. Misra, Experimental Investigation on Friction Stir Welding of Dissimilar Aluminium Alloys, *Proc. Inst. Mech. Eng. Part E J. Process Mech. Eng.*, 2021, **235**(5), p 1545–1554
29. R. Jain, S.K. Pal, and S.B. Singh, A Study on the Variation of Forces and Temperature in a Friction Stir Welding Process: A Finite Element Approach, *J. Manuf. Process.*, 2016, **23**, p 278–286
30. R.M. Bagadi, J. Jaidi, A.V. Rao, and S.D. Meshram, Tool-pin Profile Effects on Thermal and Material Flow in Friction Stir Butt Welding of AA2219-T87 Plates: Computational Fluid Dynamics Model Development and Study, *Int. J. Adv. Manuf. Technol.*, 2024, **131**, p 1–16
31. K. Elangovan and V. Balasubramanian, Influences of Tool Pin Profile and Tool Shoulder Diameter on the Formation of Friction Stir Processing Zone in AA6061 Aluminium Alloy, *Mater. Des.*, 2008, **29**(2), p 362–373
32. K. Elangovan and V. Balasubramanian, Influences of Tool Pin Profile and Welding Speed on the Formation of Friction Stir Processing Zone in AA2219 Aluminium Alloy, *J. Mater. Process. Technol.*, 2008, **200**(1–3), p 163–175
33. J.S.K. Nishant and P. Prakash, Numerical Analyses of Underwater Friction Stir Welding Using Computational Fluid Dynamics for Dissimilar Aluminum Alloys, *J. Mater. Eng. Perform.*, 2023 <https://doi.org/10.1007/s11665-023-08824-2>
34. M. Ghaffarpour, B.M. Dariani, A. Hossein Kokabi, and N.A. Razani, Friction Stir Welding Parameters Optimization of Heterogeneous Tailored Welded Blank Sheets of Aluminium Alloys 6061 and 5083 Using Response Surface Methodology, *Proc. Inst. Mech. Eng. Part B J. Eng. Manuf.*, 2012, **226**(12), p 2013–2022
35. S. Muthukumaran and S.K. Mukherjee, Multi-layered Metal Flow and Formation of Onion Rings in Friction Stir Welds, *Int. J. Adv. Manuf. Technol.*, 2008, **38**, p 68–73
36. P. Prakash, S.K. Jha, and S.P. Lal, Effect of Tool-Pin Profile on Weld Zone and Mechanical Properties in Friction Stir Welding of Aluminium Alloy, *Pertanika J. Sci. Technol.*, 2018, **26**(2), p 853–862
37. R. Nandan, G.G. Roy, and T. Debroy, Numerical Simulation of Three-dimensional Heat Transfer and Plastic Flow During Friction Stir Welding, *Metall. Mater. Trans. A*, 2006, **37**, p 1247–1259
38. V.R. Kishore, J. Arun, R. Padmanabhan, and V. Balasubramanian, Parametric Studies of Dissimilar Friction Stir Welding Using Computational Fluid Dynamics Simulation, *Int. J. Adv. Manuf. Technol.*, 2015, **80**(1–4), p 91–98
39. P. Prakash, R.S. Anand, and S.K. Jha, Prediction of Weld Zone Shape with Effect of Tool Pin Profile in Friction Stir Welding Process, *J. Mech. Sci. Technol.*, 2020, **34**, p 279–287
40. P. Prakash, S.K. Jha, and S.P. Lal, Numerical Investigation of Stirred Zone Shape and Its Effect on Mechanical Properties in Friction Stir Welding Process, *Weld. World*, 2019, **63**, p 1531–1546

41. M. Zhai, C. Wu, and H. Su, Influence of Tool Tilt Angle on Heat Transfer and Material Flow in Friction Stir Welding, *J. Manuf. Process.*, 2020, **59**, p 98–112
42. C.L. Yang, C.S. Wu, and X.Q. Lv, Numerical Analysis of Mass Transfer and Material Mixing in Friction Stir Welding of Aluminum/Magnesium Alloys, *J. Manuf. Process.*, 2018, **32**, p 380–394
43. C. Hamilton, M. Kopyściański, A. Węglowska, A. Pietras, and S. Dymek, Modeling, Microstructure, and Mechanical Properties of Dissimilar 2017A and 5083 Aluminum Alloys Friction Stir Welds, *Proc. Inst. Mech. Eng. Part B J. Eng. Manuf.*, 2019, **233**(2), p 553–564
44. R.S. Anand, P. Prakash, S.K. Jha, and A.K. Singh, Numerical Investigations of Effect of Input Process Parameters on Heat Generation in Friction Stir Welding, *Mater. Today Proc.*, 2020, **33**, p 5354–5361
45. A.K. Kadian and P. Biswas, The Study of Material Flow Behaviour in Dissimilar Material FSW of AA6061 and Cu-B370 Alloys Plates, *J. Manuf. Process.*, 2018, **34**, p 96–105
46. R.V. Padmanaban, V.R. Kishore, and V. Balusamy, Numerical Simulation of Temperature Distribution and Material Flow During Friction Stir Welding of Dissimilar Aluminum Alloys, *Procedia Eng.*, 2014, **97**, p 854–863
47. M. Selvaraj, V. Murali, and S.R. Koteswara Rao, Mechanism of Weld Formation During Friction Stir Welding of Aluminum Alloy, *Mater. Manuf. Processes*, 2013, **28**(5), p 595–600
48. N. Gotawala and A. Shrivastava, Analysis of Material Distribution in Dissimilar Friction Stir Welded Joints of Al 1050 and Copper, *J. Manuf. Process.*, 2020, **57**, p 725–736
49. P. Pankaj, A. Tiwari, L.N. Dhara, and P. Biswas, Multiphase CFD Simulation and Experimental Investigation of Friction Stir Welded High Strength Shipbuilding Steel and Aluminum Alloy, *CIRP J. Manuf. Sci. Technol.*, 2022, **39**, p 37–69
50. H. Schmidt, J. Hattel, and J. Wert, An Analytical Model for the Heat Generation in Friction Stir Welding, *Modell. Simul. Mater. Sci. Eng.*, 2003, **12**(1), p 143
51. G. Chen, Z. Feng, Y. Zhu, and Q. Shi, An Alternative Frictional Boundary Condition for Computational Fluid Dynamics Simulation of Friction Stir Welding, *J. Mater. Eng. Perform.*, 2016, **25**, p 4016–4023
52. K.K. Kumar, A. Kumar, and K. Nagu, Mechanical and Corrosion Behaviour of Friction Stir Welded 5083–6061 Aluminium Alloy Joints: Effect of Base Material Position, *Trans. Indian Inst. Metals.*, 2023, **76**(7), p 1985–1996

Publisher's Note Springer Nature remains neutral with regard to jurisdictional claims in published maps and institutional affiliations.

Springer Nature or its licensor (e.g. a society or other partner) holds exclusive rights to this article under a publishing agreement with the author(s) or other rightsholder(s); author self-archiving of the accepted manuscript version of this article is solely governed by the terms of such publishing agreement and applicable law.